HIGH AND DRY

New Observations of Tropospheric and Cloud Properties above the Greenland Ice Sheet

BY MATTHEW D. SHUPE, DAVID D. TURNER, VON P. WALDEN, RALF BENNARTZ, MARIA P. CADEDDU, BENJAMIN B. CASTELLANI, CHRISTOPHER J. COX, DAVID R. HUDAK, MARK S. KULIE, NATHANIEL B. MILLER, RYAN R. NEELY III, WILLIAM D. NEFF, AND PENNY M. ROWE

ICECAPS is a new observational campaign to study how the cloudy atmosphere impacts the energy and hydrological budgets of the central Greenland Ice Sheet.

Clouds and the atmospheric state play fundamental roles in the cryospheric mass budget of the Greenland Ice Sheet (GIS) both as a source, via precipitation, and a potential sink, via modulation of the surface energy budget. The Arctic is changing rapidly (Stroeve et al. 2007; Zhang et al. 2008; McPhee et al. 2009), and with it the GIS is losing mass at an accelerating rate (Rignot and Kanagaratnam 2006; Tedesco 2006; Hanna et al. 2008). With a total of 7 m of equivalent sea level rise captive in the GIS (Church et al. 2001), any significant loss can have dramatic implications for ▶

The Mobile Science Facility housing ICECAPS instruments at Summit, Greenland.

global coastal ecosystems and communities (FitzGerald et al. 2008; Nicholls and Cazenave 2010); may impact the thermohaline circulation, which transports global heat (Fichefet et al. 2003; Ridley et al. 2005; Jungclaus et al. 2006); and can affect other regional and global climate processes. To understand present and future manifestations of change to the GIS requires an explicit understanding of regional cloud and atmosphere processes, including how these processes interact with the ice sheet and how they might change as their environment changes.

Harsh conditions and remoteness have hindered the kind of intensive, comprehensive multisensor ground-based observations that are needed to well characterize Arctic cloud and atmospheric processes, particularly over the GIS. Sophisticated cloud–atmosphere observatories have been established at a few Arctic locations for long-term and short-term campaigns. To date, however, there have been few such observations over the GIS. For example, our knowledge of GIS clouds is limited to periodic surface observer records (e.g., Putnins 1970), approximately one year of ceilometer measurements over the central ice sheet (Starkweather 2004), and satellite measurement records (Cawkwell and Bamber 2002; Griggs and Bamber 2008). The first of these is limited in its ability to characterize the details necessary to quantify important radiative and precipitation processes. Satellite observations, while an important additional perspective, struggle to distinguish clouds from the highly reflective ice sheet surface (e.g., Curry et al. 1996), have poor thermal contrast (Frey et al. 2008), suffer from attenuation (Vaughan et al. 2009), or fail to detect frequent near-surface clouds (Marchand et al. 2008). Additionally, satellite measurements are generally temporally sparse and are unable to capture the diurnal evolution of cloud and atmospheric structure. These various limitations, in the face of such an important need, have motivated the creation of a new cloud–atmosphere observatory at Summit Station, in the center of the GIS.

AFFILIATIONS: Shupe, Castellani, and Neely—Cooperative Institute for Research in Environmental Sciences, University of Colorado, and NOAA Earth System Research Laboratory, Boulder, Colorado; Turner—NOAA/National Severe Storms Laboratory, Norman, Oklahoma; Walden, Cox, and Rowe—University of Idaho, Moscow, Idaho; Bennartz, Kulie, and Miller—University of Wisconsin—Madison, Madison, Wisconsin; Cadeddu—Argonne National Laboratory, Argonne, Illinois; Hudak—Environment Canada, King City, Ontario, Canada; Neff—NOAA/Earth System Research Laboratory, Boulder, Colorado
CORRESPONDING AUTHOR: Dr. Matthew D. Shupe, R/PSD3, 325 Broadway, Boulder, CO 80305
E-mail: matthew.shupe@noaa.gov

The abstract for this article can be found in this issue, following the table of contents.
DOI:10.1175/BAMS-D-11-00249.1

In final form 2 July 2012

THE OBSERVATORY. Covering 1.7×10^6 km^2 of Earth, the GIS is a distinctive feature of Northern Hemisphere topography. Its size and height have a significant influence on regional and Northern Hemisphere synoptic flow (e.g., Putnins 1970; Scorer 1988; Doyle and Shapiro 1999; Steffen and Box 2001). Summit Station (72.6°N, 38.5°W) is located high atop the GIS at an elevation of 3,250 m above sea level (Fig. 1), making it a unique location for a cloud–atmosphere observatory. The station is about 400 km from the east and west coastlines and more than 1,000 km from the southwest and southeast coasts, from which most of the flow impinging on Summit originates (Steffen and Box 2001; Schuenemann et al. 2009), making it a distinctly continental environment. Additionally, the high altitude leads to extremely cold and dry conditions and a relative compression of the troposphere above the ice sheet.

Initially the site of the Greenland Ice Sheet Project 2 (GISP2; e.g., Alley et al. 1996) ice core drilling station in 1989, by the mid-1990s Summit had transitioned into a hub for regional science projects to study a variety of atmosphere and ice sheet properties. Predominantly supported by the U.S. National Science Foundation, Summit has been a year-round observatory since 2003. The U.S. National Oceanic and Atmospheric Administration (NOAA) has maintained a long-term presence at the site, conducting routine measurements there since the mid-1990s. Recent and ongoing measurements at Summit examine surface–atmosphere exchange, near-surface chemistry, trace gases, surface energy and precipitation budgets, low atmosphere structure, ice core profiles, and others.

It is within this context that the Integrated Characterization of Energy, Clouds, Atmospheric State and Precipitation at Summit (ICECAPS) project began as part of the U.S. Arctic Observing Network (AON) in the spring of 2010. ICECAPS represents the most comprehensive effort to date to study the atmospheric structure and clouds at Summit, or at any other location over the GIS. The instrument suite has been intentionally modeled af-

ter other long-term Arctic observatories (e.g., Fig. 1) operated by the U.S. Department of Energy (DOE) Atmospheric Radiation Measurement Program (ARM) in Barrow, Alaska (Stamnes et al. 1999), and the NOAA–Canadian Network for Detection of Atmospheric Change (CANDAC) in Eureka, Canada (Shupe et al. 2011). Additionally, similar observational suites were deployed for shorter campaigns over the central Arctic during the Surface Heat Budget of the Arctic Ocean (SHEBA; Uttal et al. 2002) and Arctic Summer Cloud Ocean Study (ASCOS; Tjernström et al. 2012) projects. One strength of the instrument suite installed at Summit, and the other Arctic observatories, is the complementary nature of the different instruments that together provide observations to characterize most important properties of clouds, atmospheric thermodynamic state, and radiation above the site. Year-round measurements from such complex suites of instruments require the consistent and continual support and infrastructure that is provided by a facility like Summit Station. Instrument specifications and operation considerations are briefly outlined below and summarized in Table 1 and pictorially represented in Fig. 2.

One objective of the ICECAPS campaign is to characterize the atmospheric state. This is partially accomplished by a twice-daily radiosonde program. The first year of soundings measured only pressure, temperature (T), and relative humidity (RH); however, in summer 2011 the program added once-per-day radiosonde measurements of horizontal wind speed and direction. All soundings are automatically uploaded to the Global Telecommunication System for routine ingest by operational models and easy access to consumers of sounding observations. Atmospheric temperatures are also constrained by measurements near 60 GHz from the Humidity and Temperature Profiler (HATPRO) microwave radiometer (MWR; Rose et al. 2005) and spectral infrared measurements by the Polar Atmospheric Emitted Radiance Interferometer (P-AERI; Knuteson et al. 2004). These passive measurements contain information on temperature and moisture profiles at better than 5-min temporal resolution up to heights of 2–3 km above ground level (Turner et al. 2000; Crewell and Löhnert 2007; Löhnert et al. 2008, 2009). Additionally, microwave measurements at 20–30 GHz are used to derive the column-integrated precipitable water vapor (PWV) amount (Turner et al. 2007a). Information on the boundary layer depth and structure is determined from atmospheric density gradients observed using sound waves transmitted by a bistatic sodar (Neff et al. 2008).

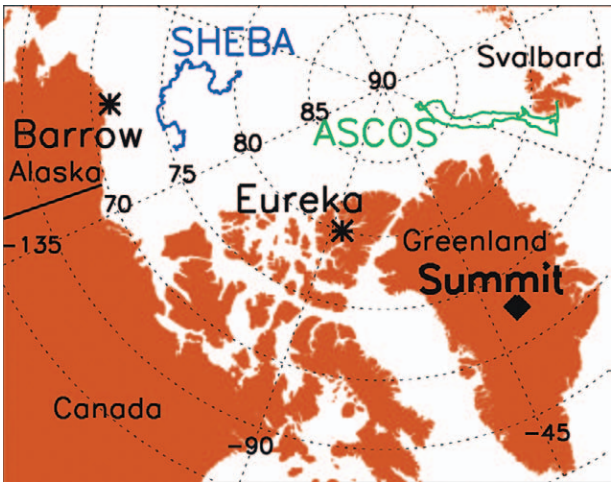

Fig. 1. Map of the Arctic showing the location of Summit, Greenland relative to other similarly instrumented Arctic observatories or campaigns.

Cloud properties are observed by a number of active and passive sensors. Two depolarization lidars are in operation: the MicroPulse Lidar (MPL; Campbell et al. 2002; Flynn et al. 2007) and the Cloud Aerosol Polarization and Backscatter Lidar (CAPABL; Neely et al. 2012, manuscript submitted to *J. Atmos. Oceanic Technol.*). Lidar backscatter is proportional to the total area of atmospheric targets (i.e., cloud particles), while the depolarization ratio contains information on particle shape (i.e., Sassen 1974; Intrieri et al. 2002), both of which are very useful in identifying particle phase. In addition, lidar measurements are used to derive cloud presence, base height, optical depth in some conditions, and microphysical properties such as particle size and water content (e.g., Donovan and van Lammeren 2001; Turner and Eloranta 2008). The lidar signal fully attenuates in clouds with optical depths greater than ~3 (Sassen and Cho 1992), preventing some upper-level observations. A ceilometer, which robustly measures the cloud-base height, augments the other lidars.

Observations from a Doppler 35-GHz Millimeter Cloud Radar (MMCR; Moran et al. 1998) nicely complement those from the lidars. Radar reflectivity and mean Doppler velocity provide information on the size and vertical motions of hydrometeors, while the Doppler spectrum width carries information on atmospheric turbulence. Cloud radar measurements contribute to the characterization of cloud presence, boundaries, phase (Shupe 2007; Luke et al. 2010), microphysical properties (Fox and Illingworth 1997; Shupe et al. 2005), and some in-cloud dynamical properties (Kollias et al. 2001; Shupe et al. 2008). Augmenting the cloud radar is a Precipitation

Occurrence Sensor System (POSS; Sheppard and Joe 2008), which is a bistatic, continuous wave, X-band radar that measures backscatter within a single sample volume a few meters above the surface. These measurements offer estimates of both the ice particle size distribution and snowfall rate.

Passive measurements of downwelling atmospheric radiation at different frequencies add further information on cloud properties. Microwave brightness temperature measurements from HATPRO and a high-frequency microwave radiometer (MWRHF) at 23, 31, 90, and 150 GHz are used to derive the column-integrated liquid water path (LWP; Turner et al. 2007a), with the higher-frequency measurements providing crucial information at the typical low liquid water amounts in the GIS environment (Crewell and Löhnert 2003). P-AERI infrared radiances nicely complement the microwave measurements by providing increased sensitivity and decreased uncertainty for LWP retrievals in optically thin clouds (Mahesh et al. 2001a,b; Turner 2005). For optimal retrievals of LWP across the range of possible values, these microwave and infrared retrievals are combined (Turner 2007). The spectral infrared measurements

Table 1. ICECAPS instrument specifications, measurements, and derived parameters. All instruments other than the IcePIC and radiosondes are pointed approximately in the zenith direction. Instrument resolutions are given as "res."

Instrument name	Key specifications	Primary measurements	Derived parameters	Institution
P-AERI	530–3,000 cm^{-1} (3–19 μm), 1 cm^{-1} res., <1-min time res.	Downwelling spectral infrared radiance	Cloud phase and microphysics, atmospheric temperature	University of Idaho
MWRHF	Frequencies: 90, 150 GHz, 2–4-s time res.	Downwelling brightness temperatures	Cloud LWP, PWV	University of Wisconsin
HATPRO	Frequencies: 7 channels 22–32 GHz, 7 channels 51–58 GHz, 2–4-s time res.	Downwelling brightness temperatures	Cloud LWP, PWV, atmospheric temperature	University of Wisconsin
MMCR	Ka band (35 GHz), 8-mm wavelength, 2-s time res., 45-m vertical res.	Reflectivity, mean Doppler velocity, Doppler spectrum width, Doppler spectra	Cloud boundaries, phase, microphysics; cloud-scale dynamics	NOAA Earth System Research Laboratory (ESRL)
MPL	532-nm wavelength, 5-s time res., 15-m vertical res., 2°–4° off zenith	Relative backscatter, hybrid linear–circular depolarization ratio	Cloud-base height, phase, microphysics	DOE ARM
CAPABL	523-nm wavelength, 15-s time res., 30-m vertical res., three-channel receiver, 2°–11° off zenith	Backscatter, linear depolarization ratio, diattenuation	Cloud-base height, phase, microphysics	NOAA/ESRL
Ceilometer	905-nm wavelength, 15-m vertical res., 15-s time res.	Backscatter	Cloud-base height	DOE ARM
POSS	X-band (10.5 GHz), 1-min time res., single volume near surface	Reflectivity, Doppler spectra	Precipitation rate	Environment Canada
Sodar	2,100 Hz, <1-m vertical res., 1-s time res.	Reflectivity	Boundary layer depth	NOAA/ESRL
IcePIC	Canon D50 DSLR, ~5.6 magnification, 1.5 μm res., 6.1 megapixels	Digital photographs	Ice crystal habit	University of Idaho
Radiosondes	1-s time res., twice daily, RS-92K or RS-92SGP sondes	Temperature, relative humidity, pressure, winds	Cloud temperature, tropospheric thermodynamic structure	University of Idaho and University of Colorado

also contain information on cloud phase (Rathke et al. 2002; Turner et al. 2003; Turner and Eloranta 2008), emissivity (Mahesh et al. 2001a,b), and some layer-averaged microphysical and optical properties (Turner 2005).

ICECAPS equipment also includes an ice particle imaging camera (IcePIC) that was patterned after one developed by Kenneth G. Libbrecht. It is a manual device with which falling ice crystals are captured on a microscope slide and photographed using a Nikon D50 DSLR camera mounted on a ~5.6X magnifying microscope body. While not quantitative in nature, these photos are useful for determining precipitating crystal habits, which are related to specific cloud conditions, and the occurrence of rime, or water droplets that freeze onto ice crystals as they fall.

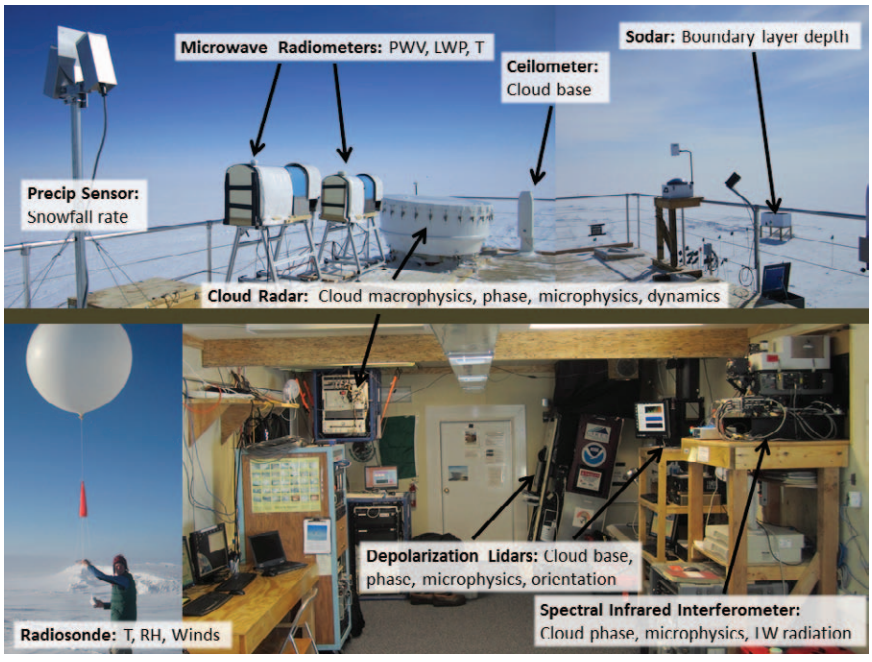

Fig. 2. Collage showing the ICECAPS instrumentation installed inside, on top of, and near the Mobile Science Facility at Summit, Greenland. LW = longwave. (Photo credits: M. Shupe, M. Okrazewski.)

Many details of the ICECAPS raw observations, derived products, and data availability are provided on the Advanced Cooperative Arctic Data and Information Service (ACADIS; www.aoncadis.org) data portal. Additionally, quicklook imagery from all data streams is updated daily on the ICECAPS website (www.esrl.noaa.gov/psd/arctic/observatories/summit).

COMPLEMENTARY PERSPECTIVES. An observational case from 21 September 2010 is used to illustrate the complementary nature of ICECAPS observations and derived products for characterizing cloud, precipitation, and atmospheric structure. On this day, a high pressure system sat directly over the central GIS leading to weak (~5 m s^{-1}) southwesterly winds at Summit. The synoptic structure is relatively steady over the couple of days surrounding this weather event, with low-level temperatures remaining near –20°C for the duration.

Active and passive remote sensors (Figs. 3–5) paint a consistent and detailed picture of cloud and atmosphere structure for this day. First, it is apparent that there are clouds overhead throughout the day. These clouds are typically decoupled from the surface by a relatively weak (<5°C) surface-based temperature inversion below 100 m. Initially, a mixed-phase stratocumulus cloud is present below 1 km while a thin cirrus cloud, composed solely of ice crystals, develops overhead. In time, the cirrus layer deepens and lowers and by 1200 UTC the stratocumulus has diminished while very light snow falls from the upper ice cloud down to the surface. The deeper, precipitating ice cloud persists until about 2100 UTC with periodic embedded layers of supercooled liquid water. Finally, after 2100 UTC the strongest, though still relatively weak, precipitation occurs as a classic multilayer, mixed-phase cloud system (e.g., Curry et al. 1996) and persists until the end of the day. Here we highlight many of the specific observational signatures that support this general picture.

We first consider the identification of condensed liquid during this case. Generally cloud liquid water is characterized by high lidar backscatter, low depolarization ratio, and a cloud base that is readily observed by ceilometer. As convection is limited in Arctic environments, liquid water usually occurs as stratiform layers. A number of these layers are clearly visible throughout the case, including at the top of stratocumulus layers at the beginning and end of the case, as well as intermittent layers embedded in a deeper cloud system in the middle (Figs. 3d,e). At times signal attenuation in lower clouds prevents the lidars from observing upper cloud layers.

Other measurements support these lidar observations and provide additional insight. For example, as the stratocumulus liquid cloud base slowly lifts from 0.5 km at 0600 UTC to 1 km by 1100 UTC, it thins geometrically (Fig. 3a). Over this same time, the microwave-derived LWP decreases from 50 g m^{-2} down to negligible values (Fig. 4d). P-AERI infrared spectra indicate initial blackbody conditions with 11-μm emissivity near unity (Figs. 5b,c), but as the cloud thins to LWP <~30 g m^{-2} the atmospheric "windows" at <600 and 750–1,250 cm^{-1} slowly open (Fig. 5a) and cloud emissivity decreases (Fig. 5b). Similar radiometric signatures indicate that liquid layers in the latter half of the case are quite thin. Finally, the 2320 UTC radiosonde profile clearly reveals water-saturated layers at 0.7 and 2 km collocated with temperature inversions at –18° to –28°C (Fig. 6). The upper cloud layer is associated with a shallow moisture inversion and its top extends into the temperature inversion (e.g., Sedlar et al. 2012; Solomon et al. 2011).

The complementary ICECAPS instrument suite provides significant information on the atmospheric thermodynamic and dynamic structure, which is closely related to the occurrence of liquid water. High temporal variability in mean Doppler velocity and wide spectrum widths (Figs. 3b,c) indicate areas of significant turbulence (O'Connor et al. 2005; Shupe et al. 2008). These areas are usually associated with supercooled liquid water layers and their turbulence production driven by cloud-top radiative cooling (e.g., Pinto 1998). The 2320 UTC sounding clearly shows mixed layers—or layers of approximately constant equivalent potential temperature—associated with both liquid cloud layers, while the 1114 UTC sounding shows a remnant of a mixed layer associated with the stratocumulus that had just passed (Fig. 6). Both soundings indicate an energetic decoupling between surface and cloud layers, characterized by surface-based temperature inversions. Water vapor mixing ratio profiles show strong moisture inversions above the surface, suggesting that advection aloft is the moisture source for the cloud. Indeed, forecast simula-

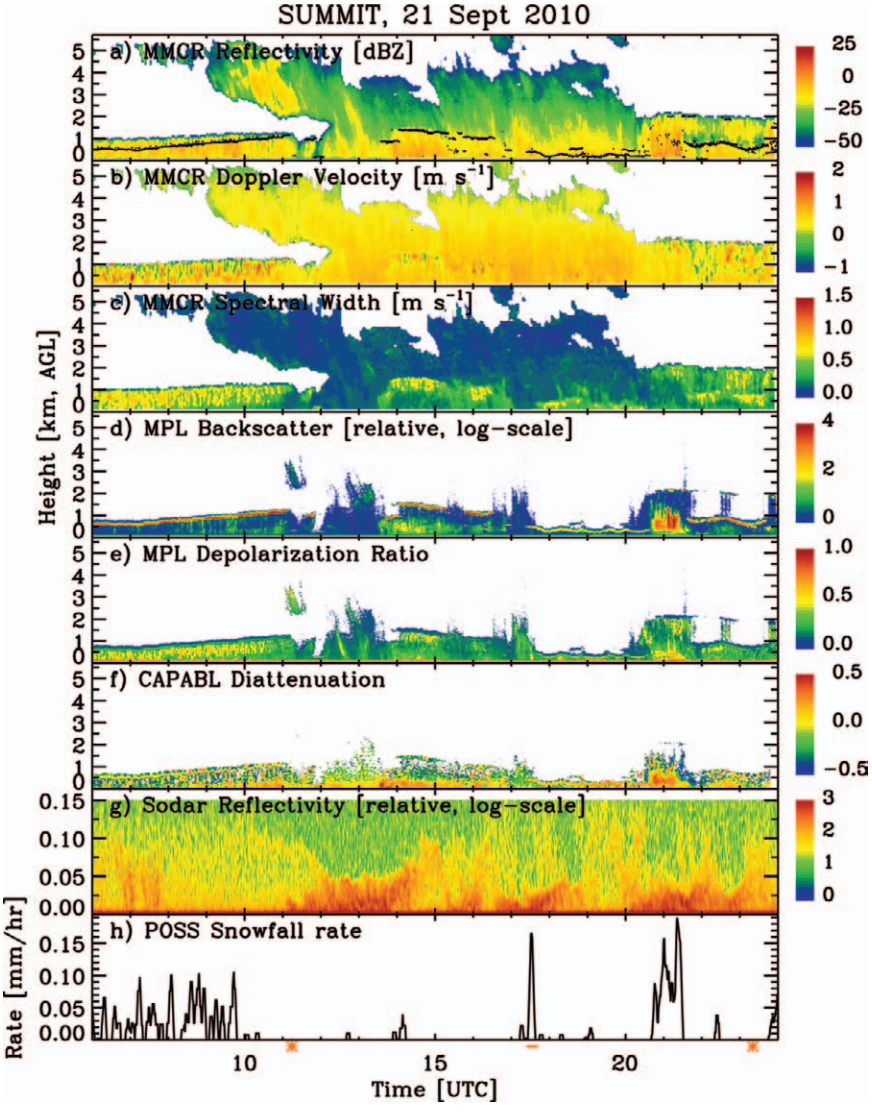

Fig. 3. Active remote-sensor measurements on 21 Sep 2010, including time–height cross sections of (a) radar reflectivity, (b) mean Doppler velocity, (c) Doppler spectrum width, (d) lidar backscatter, (e) depolarization ratio, (f) diattenuation, (g) sodar reflectivity, and (h) a time series of POSS-derived snowfall rate. The ceilometer-observed cloud-base heights are given as black dots in (a). Orange stars along the abscissa designate the time of radiosonde launches shown in Fig. 6. The orange bar along the abscissa designates the time during which photos were taken using the IcePIC in Fig. 8.

tions from the European Centre for Medium-Range Weather Forecasts (ECMWF) operational model reveal a moisture plume extending from the southern coast of Greenland up onto the GIS toward Summit (Fig. 7).

The sodar record (Fig. 3g) reveals periods of increased, near-surface static stability, characterized by higher backscatter, with the development of associated shallow mixing layers up to 25–50 m above the surface. At these times, measurements at 2 and 10 m show cooling temperatures and transitions from near-isothermal conditions to an inversion of about 2°C. These periods of increased static stability are associated with decreases in downwelling IR brightness temperatures and diminishing cloud-driven turbulence, both of which are directly linked to the thinning and/or disappearance of liquid cloud layers aloft. These interactions suggest the importance of cloud radiative and dynamical processes in the near-surface structure and surface energy budget.

The remote sensors indicate cloud ice crystals in two distinct environments. First, ice forms in and falls below the supercooled (~ –24°C) liquid water stratocumulus layers, as identified by high radar reflectivity, relatively lower lidar backscatter, and higher depolarization ratio (Figs. 3a,d,e). The streaky nature of radar reflectivity is a signature of high variability in ice related to variability of in-cloud vertical motions. Second, the higher clouds extending above 5 km are composed of ice.

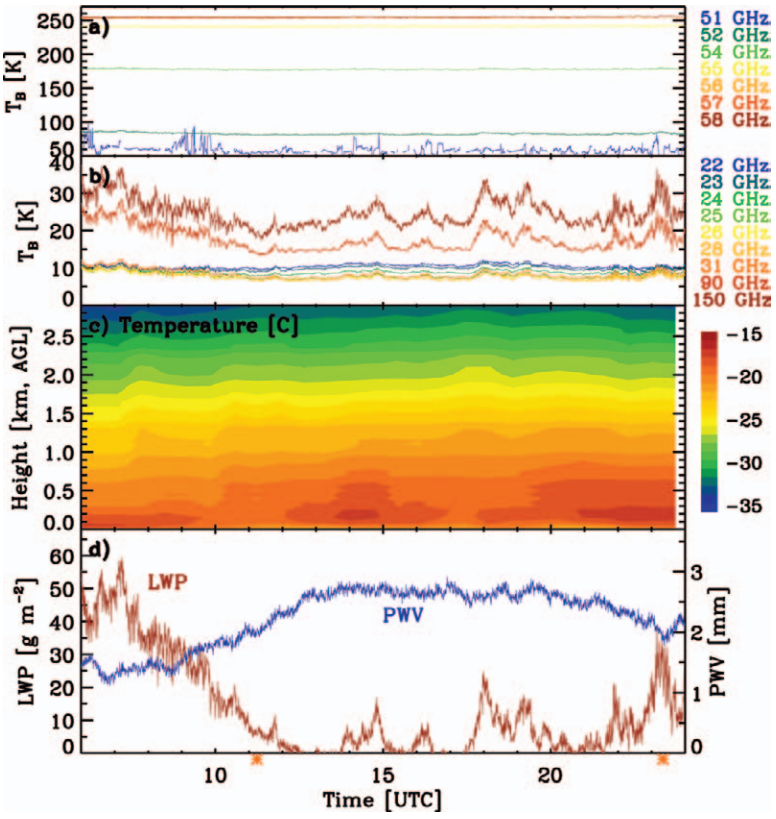

Fig. 4. Microwave radiometer measurements and retrieved parameters on 21 Sep 2010, including (a) brightness temperatures from HATPRO, (b) brightness temperatures from MWRHF, (c) atmospheric temperature profiles derived from HATPRO, and (d) cloud LWP and total PWV derived from MWRHF. Orange stars along the abscissa designate the time of radiosonde launches shown in Fig. 6.

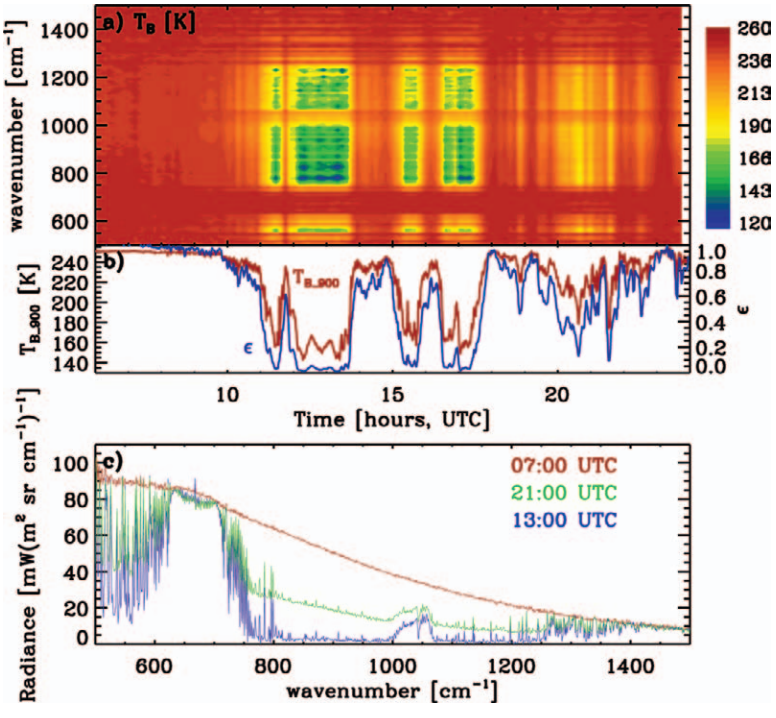

Fig. 5. P-AERI measurements and derived products on 21 Sep 2010, including (a) spectral IR brightness temperatures as a function of time, (b) time series of sky brightness temperature at 900 cm^{-1} and the derived cloud emissivity, and (c) example IR spectra under different conditions during the case.

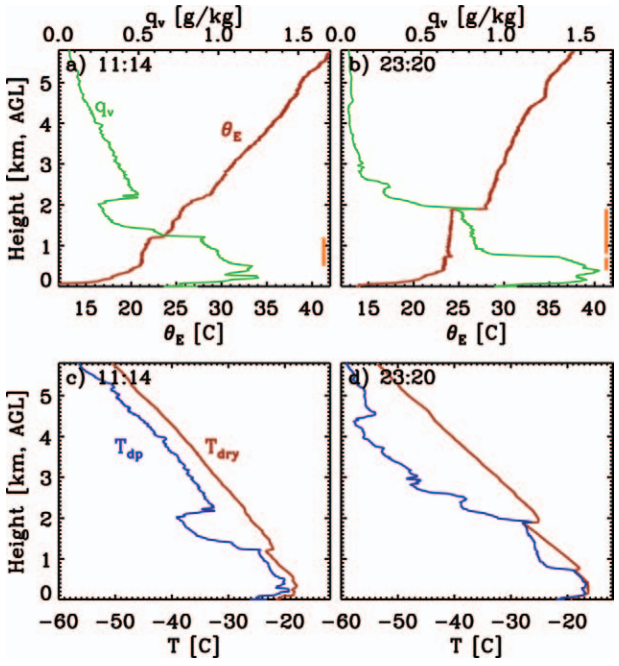

Fig. 6. Radiosonde measurements at 1114 and 2320 UTC 21 Sep 2010 of (a),(b) water vapor mixing ratio and equivalent potential temperature, and (c),(d) dry and dewpoint temperatures. The single orange bar in (a) indicates the location of a layer that was likely well mixed at some point before the sounding. The two vertical orange bars in (b) indicate well-mixed layers as identified by equivalent potential temperature.

Upper-level ice clouds typically have a jagged top, smoothly increasing radar Doppler velocity as ice particles grow with descending height, and a narrow radar spectrum width that indicates little turbulence and single-phase conditions. During the period from 1200 to 1400 UTC, when the lidars identify no liquid layers, the LWP indeed shows no liquid water in this 4-km-thick layer of ice. Lastly, radiosondes suggest cloud-top temperatures colder than –40°C (Fig. 6), a temperature range in which liquid water cannot persist (e.g., Mason 1952).

IcePIC pictures at 1740 UTC (Fig. 8) show unrimed hollow capped columns, isolated bullets, bullet rosettes, plates, and radiating plates. These crystals typically form at temperatures of –18° to –30°C (Magono and Lee 1966), consistent with observed cloud temperatures (Fig. 6) and minimal LWP at the time. For example, the capped columns likely formed initially as columns near water saturation at –20° to –25°C and then fell into somewhat warmer temperatures, supporting plate growth (e.g., Bailey and Hallett 2009). Additionally, Hayman and Thayer (2012) and Neely et al. (2012, manuscript submitted to *J. Atmos. Oceanic Technol.*) have preliminarily shown a correspondence between the lidar diattenuation ratio and ice crystal orientation (Fig. 3f). Higher diattenuation suggests horizontally oriented particles, while lower diattenuation suggests particle populations with randomly distributed orientation. The highest diattenuation values are found in the ice precipitating from supercooled liquid clouds, but below the turbulent mixed layers associated with these clouds. As opposed to the habits listed above that are falling from the upper ice cloud, many of which have no preferred fall orientation, it is likely that crystals formed in the mixed-phase clouds are more dendritic in nature. In nonturbulent environments, these crystals fall in a preferred horizontally aligned orientation as suggested by CAPABL. Additional work is required to understand this new type of measurement before further conclusions can be drawn (Neely et al. 2012, manuscript submitted to *J. Atmos. Oceanic Technol.*). Lastly, although the MMCR indicates ice crystals falling to the surface all day, much of this precipitation is so light that it is barely detectable by the POSS. Only during the initial stratocumulus layer and at a couple other short periods, including the period when IcePIC pictures were taken, does the POSS observe measureable precipitation at the surface (Fig. 3h).

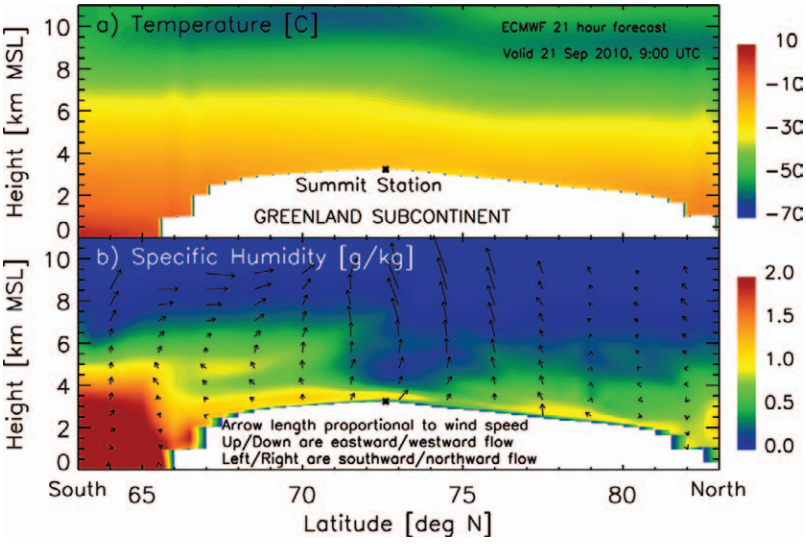

Fig. 7. 21-h forecast from the ECMWF operational model along a longitudinal slice through Summit Station of (a) temperature and (b) specific humidity and winds, valid at 0900 UTC 21 Sep 2010.

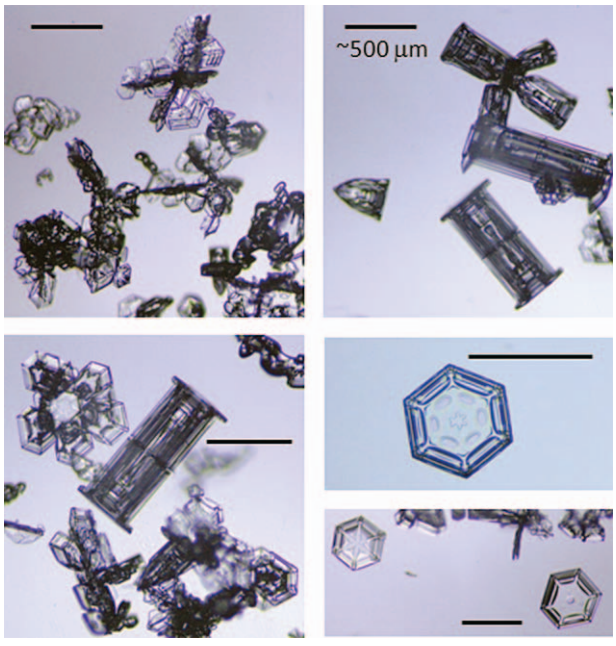

Fig. 8. IcePIC ice crystal photographs taken at 1740 UTC 21 Sep 2010. In each photograph a reference bar of 500-μm length is provided for scale.

CHARACTERISTIC CLOUD AND ATMOSPHERIC PROPERTIES. The ICECAPS measurements can be used collectively to extend well beyond specific case studies to provide a broader characterization of cloud and atmosphere properties at Summit. Fine temporal sampling can be used to develop statistical distributions of cloud and atmospheric properties over monthly and seasonal time scales. These distributions can then be used to evaluate output from numerical models, compare cloud and atmospheric state properties between different Arctic sites, and validate retrievals from satellite measurements. Analyses based on the first 20 months of observations offer many first looks into this important environment.

Atmospheric structure. The twice-daily radiosonde program represents an important contribution of ICECAPS toward understanding the basic meteorology over the GIS. While soundings have been made sporadically over the ice sheet in the past (e.g., Forrer and Rotach 1997; Helmig et al. 2002), there has never been a sounding campaign with such high temporal resolution over an extended period of time. Atmospheric temperature and moisture profiles from the first 600 days of radio soundings are depicted in Fig. 9. It is clear that, due to the high altitude at Summit, specific humidity is quite low year-round, with near-surface summer values around 2 g kg^{-1}, and winter values sometimes an order of magnitude smaller. Unique seasonal variability is observed as the tropopause height descends from a summer maximum around 6–8 km above ground level to a late-winter minimum below 5 km. This cycle is likely related to large-scale stratospheric pumping circulations between the Arctic and tropics that are strongest in winter but weaken in spring (Highwood et al. 2000). Higher-frequency variability is observed as relatively warm, moist air masses associated with regional synoptic activity impinge upon the central ice sheet every 7–10 days.

Probability density profiles representing these data offer a statistical representation of the atmospheric structure (Fig. 10). Bimodal distributions of temperature and moisture through most of the troposphere are related to synoptic-scale variability seen in Fig. 9, where warm, moist conditions are typically associated with the occurrence of clouds. In a mean sense, for both cloudy- and clear-sky conditions, there are surface-based inversions of temperature and mois-

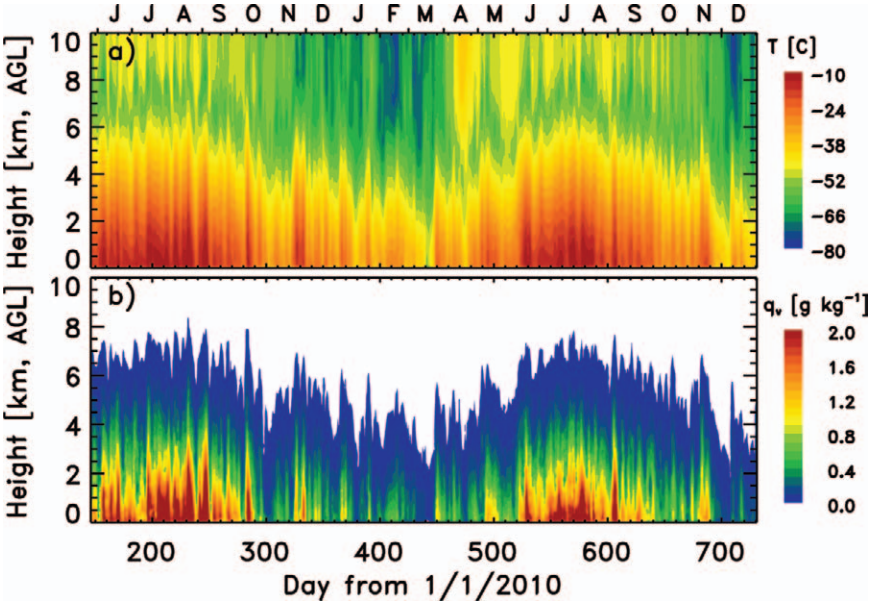

Fig. 9. Radiosonde-measured (a) temperature and (b) water vapor mixing ratio. Months are labeled along the top axis.

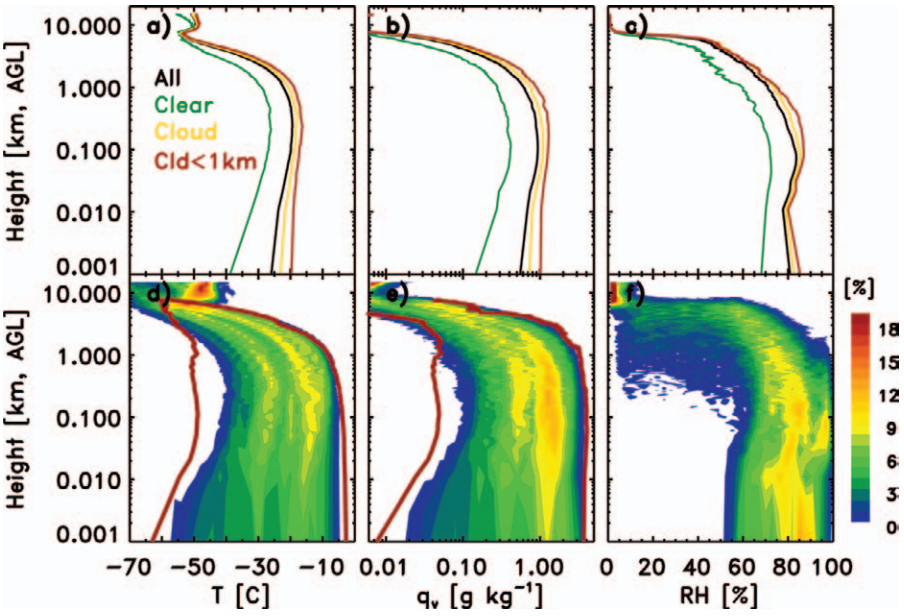

Fig. 10. Radiosonde-measured (a),(d) temperature, (b),(e) water vapor mixing ratio, and (c),(f) relative humidity. Top panels include average curves for all sky, clear sky, cloudy sky, and cloudy sky with clouds below 1 km. Bottom panels include probability density plots where probability distributions are calculated at each height. Note that (d) and (e) also include the extreme soundings based on low-level measurements: the coldest is from 17 Mar 2011, the warmest from 2 Sep 2010, the driest from 17 Mar 2011, and the wettest from 3 Sep 2010.

ture up to 100–200 m. These inversions are typically stronger under clear-sky conditions relative to cloudy skies due to extreme low near-surface values at those times. This average inversion structure, particularly for moisture, points to the importance of advection aloft as a moisture source for tropospheric processes. Additionally, the region of highest relative humidity (>95%) extends from the surface up to about 2 km, with a particularly high frequency of occurrence at 30–100 m associated with common fog layers.

Monthly statistics reveal further insight into the annual evolution of atmospheric properties (Fig. 11). Near-surface temperatures reach an annual minimum in March, with the coldest radiosonde measurement of near-surface temperature of –63.7°C on 17 March 2011 (day 441 in Fig. 9a) associated with a likely cold temperature record event at Summit. Extreme summer maximum temperatures are typically below –10°C, while the warmest temperature recorded by ICECAPS radiosondes was –2.6°C on 2 September 2010.

At least one tropospheric temperature inversion, defined here as any layer deeper than 40 m where temperature increases with height (or over any depth when starting from the surface), has been observed in every ICECAPS radio sounding except for a single profile on 6 September 2010. While there are typically two to four temperature inversions in the vertical, the first inversion almost always originates from the surface from October through March, with a gradual trend toward more elevated inversions in summer (Fig. 11b). The lowest inversion's physical depth is marginally deeper in winter relative to summer, yet the inversion strength, or temperature difference across the inversion, is dramatically stronger in winter, reaching values typically greater than 10°C over depths of about 200 m. These inversions are formed through strong radiative cooling at the surface combined with relatively warm advection aloft through most of the year. The transition toward more elevated inversions in the summer is likely due to relatively more surface heating from solar radiation and to the presence of thicker clouds that shape the thermodynamic structure via radiatively driven vertical mixing processes.

Moisture inversions are frequently concurrent with temperature inversions in winter but become less frequent in summer (Fig. 11e). In all months, it is more common to observe moisture inversions associated with surface-based temperature inversions than with those that are elevated above the surface. On average, moisture inversions stronger than 0.01 g kg^{-1} occur 97% of the time when surface-based temperature inversions are present and 47% of the time when elevated inversions are present. Finally, the annual evolution of total precipitable water vapor (Fig. 11f) follows a distinct annual cycle with values less than ~1.5 mm from October through April and substantial increases in the warmer months of the year.

These basic meteorological parameters reveal unique atmospheric seasonal regimes that are quite distinct from typical, lower-latitude seasonal definitions. Winter is characterized by cold surface temperature (<–35°C on average), frequent surface-

based temperature inversions (>90%) that are strong (>10°C), and low PWV (<1.5 mm). In contrast, summer is characterized by relatively warm surface temperature (>–15°C), few surface-based temperature inversions (<50%), weaker inversions (<5°C), and high PWV (>3 mm). Between these two extreme states there are relatively quick transitions. Defined in this way, the "summer" at Summit comprises the typical June–August time period. "Winter" is from November through March but can extend into both April and October. "Spring" is typically in May and part of April, while "autumn" is September and most of October.

The annual cycle of inversion strength and frequency of surface-based temperature inversions suggest distinct seasonal regimes of near-surface atmospheric static stability. Seasonal probability density profiles of equivalent potential temperature vertical gradient (Fig. 12) exhibit signatures of this seasonal trend. Constant equivalent potential temperature in height (i.e., gradient near zero) indicates statically near-neutral conditions, while increases in height, or positive gradients, are a clear signature of statically stable conditions. Winter radio soundings reveal strongly stable conditions near the surface up to at least 100–200 m (Fig. 12d). In the transition seasons, both of which reveal some signatures of the winter structure, probability density profiles suggest periodic near-neutral conditions. Summer radio soundings indicate frequent low-level, near-neutral conditions (values <0 K km^{-1}) with only periodic near-surface stable conditions.

Cloud structure. The cloudy atmosphere is in many ways distinct from the clear atmosphere above Summit (e.g., Fig. 10). Factors such as atmospheric static stability and moisture availability impact cloud processes and help to shape the seasonal evolution of cloud occurrence and properties over the central GIS. Clouds, defined here as hydrometeors observed by ground-based sensors above about 100 m in the atmosphere, are most frequent in the relatively warm and moist summer (Fig. 13b) when the lower troposphere is generally less stable (Fig. 12b). At this time of year, clouds are present more than 85% of the time with a typical maximum in cloudiness near the surface and decreasing cloudiness with increasing altitude (Fig. 13a). Annual minimum cloud occurrence in late winter and early spring with total monthly fractions approaching 65% under very cold

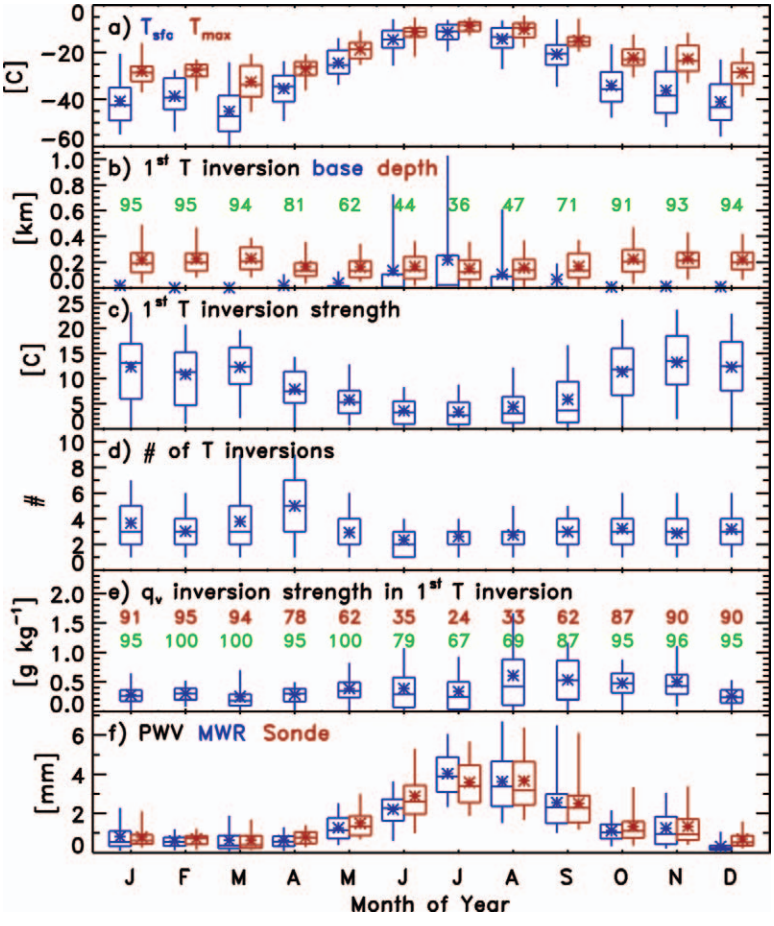

Fig. 11. Monthly statistics of (a) surface (blue) and maximum (red) atmospheric temperature, (b) base height (blue) and depth (red) of the lowest temperature inversion, (c) strength of lowest temperature inversion, (d) number of observed temperature inversions in the vertical, (e) strength of moisture inversion associated with lowest temperature inversion, and (f) PWV derived from MWR (blue) and radiosondes (red). Note that (b) includes the occurrence frequency of surface-based temperature inversions (green), and (e) includes the occurrence frequency of moisture inversions within the lowest temperature inversion (red) and within surface-based temperature inversions (green). In all cases, temperature inversions are defined based on a minimum depth of 40 m for the change into, or out of, an inversion layer. Box-and-whisker plots contain information on the 5th and 95th percentiles (ends of whiskers), 25th and 75th percentiles (ends of box), median (line in box), and mean (symbol).

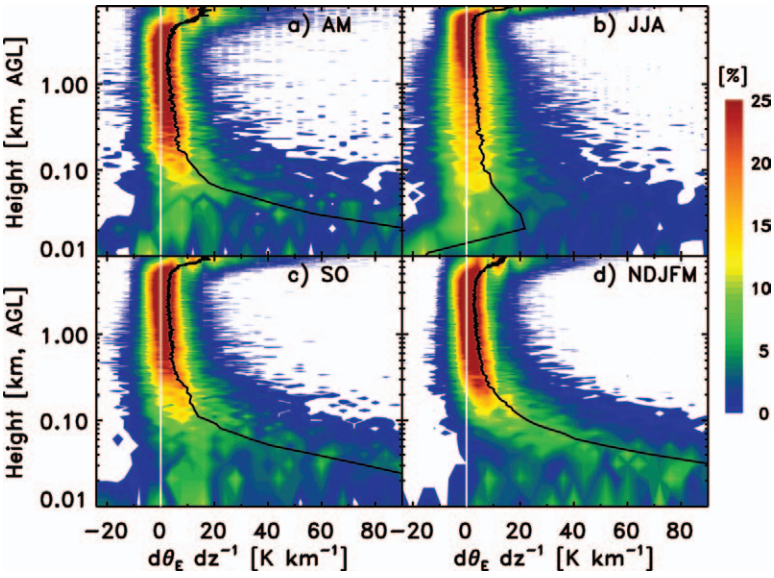

Fig. 12. Radiosonde probability density plots of the vertical gradient of equivalent potential temperature broken into site-specific seasons. Probability distributions are calculated at each height and therefore are relative to other observations at the given height. Seasonal definitions are based on distinct regimes in low-level temperature and inversion characteristics seen in Fig. 11 and discussed in the text. The solid black curve in each panel is the median profile, while the white line shows where the vertical gradient equals zero.

and dry conditions. The relatively high occurrence fractions in all seasons are similar to those observed elsewhere in the Arctic (e.g., Shupe et al. 2011) but are inconsistent with some past climatologies (e.g., Wang and Key 2005) that have suggested lower cloud occurrence fractions over Greenland than elsewhere. This discrepancy is likely due to the frequent occurrence of optically thin ice crystal layers, sometimes many kilometers thick, that may be difficult to detect by surface observers and passive satellite measurements.

The highest cloud tops tend to loosely track the tropopause height (Figs. 9a, 13c), with a dip in cloud top and total cloud depth in late winter and early spring as the tropopause lowers. The lowest cloud-base height is typically lower, on average, in summer and higher in winter, consistent with seasonal changes in low-level static stability. Similarly, the cloud liquid water path increases dramatically in July–October, a cycle that slightly lags the total available PWV. While the average LWP is very small in most other months of the year (Fig. 13e), liquid water still occurs frequently (Fig. 13b), ranging from a 10% occurrence fraction in late winter to a 40%–60% occurrence fraction in summer. These results highlight the importance of optically thin, liquid-water-containing clouds (e.g., Turner et al. 2007b), which, since they are often not opaque in the infrared, have radiative effects that are very sensitive to changes in cloud properties. Snowfall rate also reaches a maximum in midsummer and into fall (Fig. 13f), following closely the monthly variability of LWP. In all months, snowfall is relatively weak and contributes to the typical annual, water-equivalent accumulation at Summit of about 24 cm (Alley et al. 1993; Hanna et al. 2006).

To provide a first-order meteorological context for the cloud and precipitation observations at Summit, a simple analysis is performed that relates cloud and precipitation occurrence to observed 10-m wind direction measured by NOAA meteorological sensors. Clouds occur at least 60% of the time independent of low-level wind direction; however, cloud occurrence is more frequent (typically ~80% of the time) for all incident wind directions other than the northeast quadrant (Fig. 14a). For wind direction coming from this northeast quadrant, geometrically thinner clouds comprise a higher relative fraction. Precipitation, here defined based on cloud radar reflectivity thresholds, is most frequent under westerly winds and again least frequent with winds from the northeast quadrant (Fig. 14b). If surface pressure is considered in this same way (Fig. 14c), then relatively more low pressure systems occur at Summit with winds from the southeast quadrant, while generally few low pressure systems occur with westerly winds, implying that low-pressure centers typically occur to the south of Summit. Ultimately, the net distribution of observed winds determines the total amount of cloudiness that approaches Summit from each direction. As winds over this time period are strongly dominated by southwesterly flow (Fig. 14f), most clouds and precipitation observed at Summit also occur under winds from that direction (Figs. 14d,e), presumably accompanying air masses that originate in the North Atlantic.

Despite the unique environmental conditions and regional topography around Summit, many of the cloud results summarized in Fig. 13 and qualitatively observed in the data are similar to those found elsewhere in the Arctic. In particular,

low-level, stratiform mixed-phase clouds have a very similar structure to those found elsewhere. For example, Fig. 15 shows vertical probability distributions of equivalent potential temperature and specific humidity for cases with low clouds present that have a base below 1.5 km and a top below 3.0 km. Cloud top extended above the temperature inversion base in 87% of cases, while there was a moisture inversion coincident with the temperature inversion in ~75%, as has been observed at other Arctic locations (Sedlar et al. 2012). The equivalent potential temperature indicates a well-mixed layer usually encompassing at least the cloud depth and sometimes extending all the way to the surface, while more than 75% of the time the profiles suggest that the cloud mixed layer does not reach the surface (i.e., the cloud layer is decoupled from the surface). These basic structural elements are very similar to stratiform cloud structure over other locations in the Arctic (Shupe et al. 2006; Solomon et al. 2011). As Summit is distant from surface sources of heat and moisture, it is clear that these stratiform clouds maintain themselves via in-cloud processes and the long-range transport of moisture aloft (Morrison et al. 2012).

EXPLORING FUTURE POSSIBILITIES. Measurements obtained by the ICECAPS project offer new and detailed insight into the atmospheric state, cloud, radiation, and precipitation processes over the central GIS. They have revealed ways in which the atmospheric scene over the ice sheet is similar to other Arctic locations and other ways in which the clouds and atmosphere are unique. Initial analyses from the first 20 months of observations suggest a wealth of information that will be pivotal toward making significant advances in our understanding of regional cloud and atmosphere processes that are important to surface energy and mass budgets over the ice sheet. However, a great deal of research and analysis is still needed to harvest this information from the growing datasets and to coordinate the ICECAPS observations with ongoing observational and modeling efforts in the region.

A first order of business is to develop a baseline characterization of Summit's atmosphere and clouds, including detailed cloud microphysical parameters, since little is known about these properties and their annual variability. Such a characterization will help place central Greenlandic conditions within the context of those observed elsewhere in the Arctic.

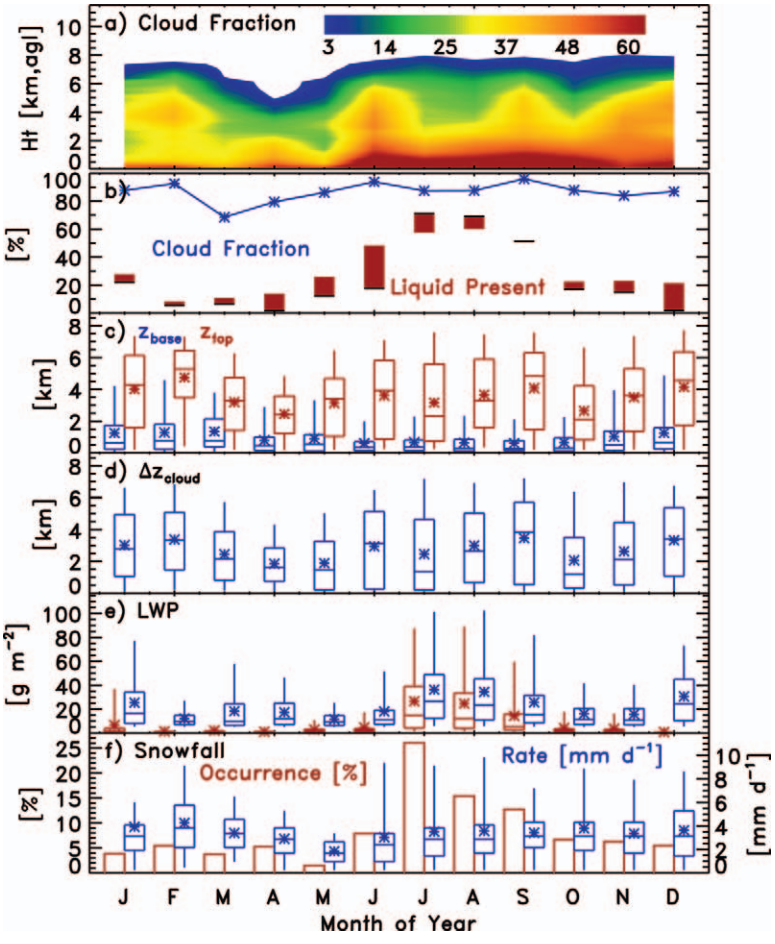

Fig. 13. Monthly statistics of (a) cloud occurrence fraction as a function of height, (b) total cloud occurrence fraction in the vertical column (blue) and the occurrence fraction of liquid water (bars indicate the range between values derived from lidar depolarization measurements and an MWR-derived LWP threshold of 5 g m^{-2} in black), (c) low cloud-base (blue) and high cloud-top (red) heights when clouds are present, (d) maximum depth over which clouds occur (high top to low base, but not necessarily cloudy throughout) when clouds are present, (e) MWR-derived LWP in all conditions (red) and in those conditions identified as cloudy with a LWP >5 g m^{-2} (blue), and (f) POSS-derived snowfall occurrence fraction (red) and liquid-equivalent snowfall rate when snow is occurring (blue). Box-and-whisker plots contain information on the 5th, 25th, 50th, 75th, and 95th percentiles and mean (symbol).

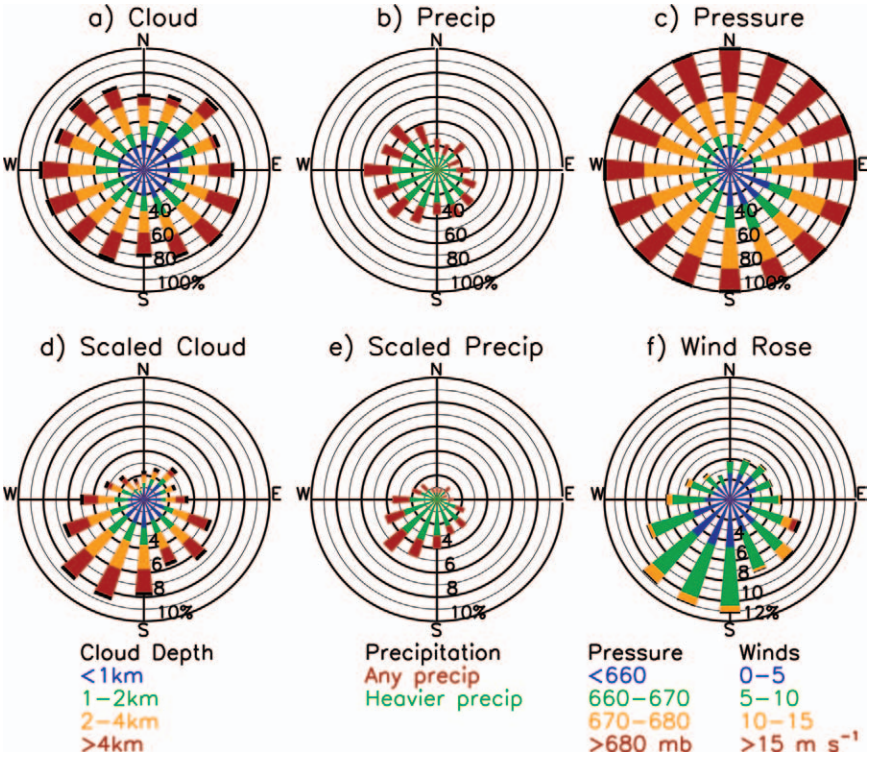

Fig. 14. Cloud and precipitation occurrence as a function of 10-m wind direction. (a) Fractional occurrence of clouds in different thickness ranges when a given wind direction occurs. (b) Fractional occurrence of precipitation of different magnitudes when a given wind direction occurs. Precipitation is identified for radar reflectivities above –5 dBZ with heavy precipitation identified above 5 dBZ. (c) Fractional occurrence of surface pressure regime when a given wind direction occurs. (d) As in (a), but scaled by the actual wind rose in (f) such that this shows the total distribution of cloud occurrence as a function of wind direction. (e) As in (d), but for precipitation. (f) The actual wind rose indicating the direction from which the wind reaches Summit in different ranges of wind speed.

They will also serve as a first means of evaluating model simulations of these properties and validating satellite observations in a complicated environment. Further, the comprehensive ICECAPS observations offer possibilities to examine atmospheric processes such as those related to cloud maintenance and phase partitioning mechanisms to determine, for example, the degree to which long-lived stratocumulus clouds over the ice sheet are similar to their counterparts that occur in other Arctic environments.

Ultimately, the detailed cloud and atmosphere information must be interpreted jointly with longer-term and ongoing measurements at Summit related to the surface energy and mass budgets. Specific details regarding collocated broadband radiation, precipitation, and atmospheric gas

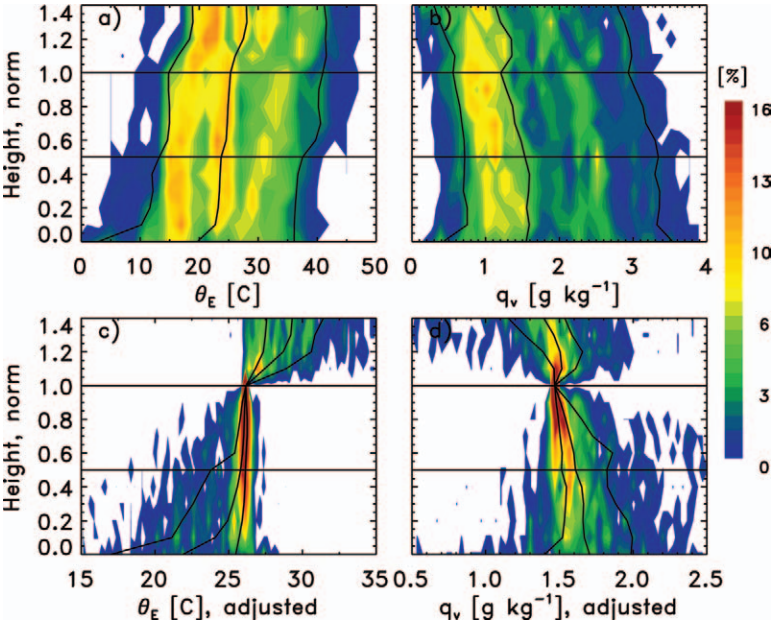

Fig. 15. Probability density profiles of radiosonde-measured (a),(c) equivalent potential temperature and (b),(d) specific humidity for stratiform cloud cases where cloud base is lower than 1.5 km, cloud top is lower than 3 km, and the temperature inversion base resides above cloud base but below cloud top plus 50 m. These conditions occur ~10% of the time. Heights have been normalized such that 0 is surface, 0.5 is cloud base, 1.0 is temperature inversion base (which in some cases is also cloud top), and 1.4 is cloud top if it extends above inversion base. Horizontal black lines denote these layers. In (c) and (d), all profiles have been linearly adjusted such that the values at the temperature inversion base (1.0) are identical. Vertical black curves in (a) and (b) represent the 5th, 50th, and 95th percentiles, while in (c) and (d) they are the 25th, 50th, and 75th percentiles.

measurements at Summit can be obtained at the GEOSummit web page (www.geosummit.org). Using the combined measurements, important questions must be answered regarding the manner in which clouds redistribute radiant energy vertically within the system, a process that is integrally connected to cloud phase and microphysical composition. Further, the surface cloud radiative forcing should be examined to determine the extent to which clouds are a net source of heat to the surface. In terms of the mass budget, precipitation processes are not well understood over the ice sheet. The ICECAPS measurements provide a path toward characterizing the relative contributions of different precipitation mechanisms to the net accumulation observed at Summit. They also offer a unique depiction of cloud and atmosphere processes that will assist in interpretation of water isotope measurements at Summit. Finally, the broader meteorological context that influences the processes observed at Summit can be better understood through coordinated interpretation and evaluation of operational models, reanalysis data, and regional mesoscale modeling.

At present the GIS is responding quickly and dramatically to the changing global climate. Detailed, process-level observations, such as those provided by the ICECAPS project at Summit, are essential to understand how the atmosphere and clouds impact these changes and responses. These detailed observations are critically needed to better constrain, evaluate, and develop models that can accurately represent climate processes in such extreme and unique environments. In the end, it will be these models that are relied upon to project the future fate of the ice sheet and its implications for global climate and ecosystems.

ACKNOWLEDGMENTS. ICECAPS is supported by the U.S. National Science Foundation under Grants ARC-0856773, 0904152, and 0856559 as part of the Arctic Observing Network (AON) program. Argonne National Laboratory's work was supported by the U.S. Department of Energy, Office of Science, under contract DE-AC02-06CH11357. Additional instrumentation support is provided by the NOAA Earth System Research Laboratory (ESRL), U.S. Department of Energy ARM Program, and Environment Canada. Low-level wind and pressure measurements were obtained from the NOAA ESRL Global Monitoring Division. Model analyses were provided by Richard Forbes at the ECMWF. We appreciate the tremendous contributions from an extensive team who have facilitated field operations, installations, instrument maintenance, and other support, including Scott Abbott, Catherine Alvarez, Raul Alvarez, Steven Bradley, Rich Coulter, Thomas Cox, Bradley Halter, Michael Hardesty, Matthew Hayman, Duane Hazen, Richard Marchbanks, Timothy Martin, Aronne Merrelli, Ken Moran, Matthew Okrazewski, Erik Olson, Micheal O'Neill, Claire Pettersen, Peter Rodriguez, Lance Roth, Scott Sandberg, Robert Stillwell, and Jeffery Thayer. ICECAPS is made possible by excellent logistical support provided by Polar Field Services, including its team of remote and on-site personnel led by Katrine Gorham; and by the Summit Science Coordination Office led by John Burkhart and Jack Dibb.

REFERENCES

Alley, R. B., and Coauthors, 1993: Abrupt increase in Greenland snow accumulation at the end of the Younger Dryas event. *Nature,* **362,** 527–529.

——, P. Mayewski, D. Peel, and B. Stauffer, 1996: Twin ice cores from Greenland reveal history of climate change, more. *Eos, Trans. Amer. Geophys. Union,* **77,** 209–210.

Bailey, M. P., and J. Hallett, 2009: A comprehensive habit diagram for atmospheric ice crystals: Confirmation from the laboratory, AIRS II, and other field studies. *J. Atmos. Sci.,* **66,** 2888–2899.

Campbell, J. R., D. L. Hlavka, E. J. Welton, C. J. Flynn, D. D. Turner, J. D. Spinhirne, V. S. Scott, and I. H. Hwang, 2002: Full-time, eye-safe cloud and aerosol lidar observation at Atmospheric Radiation Measurement Program sites: Instruments and data processing. *J. Atmos. Oceanic Technol.,* **19,** 431–442.

Cawkwell, F. G. L., and J. L. Bamber, 2002: The impact of cloud cover on the net radiation budget of the Greenland Ice Sheet. *Ann. Glaciol.,* **34,** 141–149.

Church, J. A., and Coauthors, 2001: Changes in sea level. *Climate Change 2001: The Scientific Basis,* J. T. Houghton et al., Eds., Cambridge University Press, 639–693.

Crewell, S., and U. Löhnert, 2003: Accuracy of cloud liquid water path from ground-based microwave radiometry 2. Sensor accuracy and synergy. *Radio Sci.,* **38,** 8042, doi:10.1029/2002RS002634.

——, and ——, 2007: Accuracy of boundary layer temperature profiles retrieved with multifrequency multiangle microwave radiometry. *IEEE Trans. Geosci. Remote Sens.,* **45,** 2195–2201.

Curry, J. A., W. B. Rossow, D. Randall, and J. L. Schramm, 1996: Overview of Arctic cloud and radiation characteristics. *J. Climate,* **9,** 1731–1764.

Donovan, D. P., and A. C. A. P. van Lammeren, 2001: Cloud effective particle size and water content profile retrievals using combined lidar and radar observations: 1. Theory and examples. *J. Geophys. Res.,* **106** (D21), 27 425–27 448.

Doyle, J. D., and M. A. Shapiro, 1999: Flow response to large-scale topography: The Greenland tip jet. *Tellus,* **51A,** 728–748.

Fichefet, T., C. Poncin, H. Goosse, P. Huybrechts, I. Janssens, and H. Le Treut, 2003: Implications of changes in freshwater flux from the Greenland Ice Sheet for the climate of the 21st century. *Geophys. Res. Lett.,* **30,** 1911, doi:10.1029/2003GL017826.

FitzGerald, D. M., M. S. Fenster, B. A. Argow, and I. V. Buynevich, 2008: Coastal impacts due to sea-level rise. *Annu. Rev. Earth Planet. Sci.,* **36,** 601–647.

Flynn, C. J., A. Mendoza, Y. Zheng, and S. Mathur, 2007: Novel polarization-sensitive micropulse lidar measurement technique. *Opt. Express,* **15,** 2785–2790.

Forrer, J., M., and W. Rotach, 1997: On the turbulence structure in the stable boundary layer over the Greenland Ice Sheet. *Bound.-Layer Meteor.,* **85,** 111–136.

Fox, N. I., and A. J. Illingworth, 1997: The retrieval of stratocumulus cloud properties by ground-based cloud radar. *J. Appl. Meteor.,* **36,** 485–492.

Frey, R. A., S. A. Ackerman, Y. Liu, K. I. Strabala, H. Zhang, J. R. Key, and X. Wang, 2008: Cloud detection with MODIS. Part I: Improvements in the MODIS cloud mask for Collection 5. *J. Atmos. Oceanic Technol.,* **25,** 1057–1072.

Griggs, J. A., and J. L. Bamber, 2008: Assessment of cloud cover characteristics in satellite datasets and reanalysis products for Greenland. *J. Climate,* **21,** 1837–1849.

Hanna, E., J. McConnell, S. Das, J. Cappelen, and A. Stephens, 2006: Observed and modeled Greenland Ice Sheet snow accumulation, 1958–2003, and links with regional climate forcing. *J. Climate,* **19,** 344–358.

——, and Coauthors, 2008: Increased runoff from melt from the Greenland Ice Sheet: A response to global warming. *J. Climate,* **21,** 331–341.

Hayman, M., and J. P. Thayer, 2012: General description of polarization in lidar using Stokes vectors and polar decomposition of Mueller matrices. *J. Opt. Soc. Amer.,* **29,** 400–409.

Helmig, D., J. Boulter, D. David, J. S. Birks, N. J. Cullen, K. Steffen, B. J. Johnson, and S. J. Oltmans, 2002: Ozone and meteorological boundary-layer conditions at Summit, Greenland, during 3–21 June 2000. *Atmos. Environ.,* **36,** 2595–2608.

Highwood, E. J., B. J. Hoskins, and P. Berrisford, 2000: Properties of the Arctic tropopause. *Quart. J. Roy. Meteor. Soc.,* **126,** 1515–1532.

Intrieri, J. M., M. D. Shupe, T. Uttal, and B. J. McCarty, 2002: An annual cycle of Arctic cloud characteristics observed by radar and lidar at SHEBA. *J. Geophys. Res.,* **107,** 8030, doi:10.1029/2000JC000423.

Jungclaus, J. H., H. Haak, M. Esch, E. Roeckner, and J. Marotzke, 2006: Will Greenland melting halt the thermohaline circulation? *Geophys. Res. Lett.,* **33,** L17708, doi:10.1029/2006GL026815.

Knuteson, R. O., and Coauthors, 2004: Atmospheric Emitted Radiance Interferometer. Part I: Instrument design. *J. Atmos. Oceanic Technol.,* **21,** 1763–1776.

Kollias, P., B. A. Albrecht, R. Lhermitte, and A. Savtchenko, 2001: Radar observations of updrafts, downdrafts, and turbulence in fair-weather cumuli. *J. Atmos. Sci.,* **58,** 1750–1766.

Löhnert, U., S. Crewell, O. Krasnov, E. O'Connor, and H. Russchenberg, 2008: Advances in continuously profiling the thermodynamic state of the boundary layer: Integration of measurements and methods. *J. Atmos. Oceanic Technol.,* **25,** 1251–1266.

——, D. D. Turner, and S. Crewell, 2009: Ground-based temperature and humidity profiling using spectral infrared and microwave observations. Part I: Simulated retrieval performance in clear-sky conditions. *J. Appl. Meteor. Climatol.,* **48,** 1017–1032.

Luke, E., P. Kollias, and M. D. Shupe, 2010: Detection of supercooled liquid in mixed-phase clouds using radar Doppler spectra. *J. Geophys. Res.,* **115,** D19201, doi:10.1029/2009JD012884.

Magono, C., and C. W. Lee, 1966: Meteorological classification of natural snow crystals. *J. Fac. Sci. Hokkaido Univ.,* **2,** 321–335.

Mahesh, A., V. Walden, and S. G. Warren, 2001a: Ground-based infrared remote sensing of cloud properties over the Antarctic Plateau. Part I: Cloud-base heights. *J. Appl. Meteor.,* **40,** 1265–1278.

——, ——, and ——, 2001b: Ground-based infrared remote sensing of cloud properties over the Antarctic Plateau. Part II: Cloud optical depths and particle sizes. *J. Appl. Meteor.,* **40,** 1279–1294.

Marchand, R., G. G. Mace, T. Ackerman, and G. Stephens, 2008: Hydrometeor detection using *Cloudsat*—An Earth-orbiting 94-GHz cloud radar. *J. Atmos. Oceanic Technol.,* **25,** 519–533.

Mason, B. J., 1952: The spontaneous crystallization of supercooled water. *Quart. J. Roy. Meteor. Soc.,* **78,** 22–27.

McPhee, M. G., A. Proshutinsky, J. M. Morison, M. Steele, and M. B. Alkire, 2009: Rapid change in freshwater content of the Arctic Ocean. *Geophys. Res. Lett.,* **36,** L10602, doi:10.1029/2009GL037525.

Moran, K., B. Martner, M. Post, R. Kropfli, D. Welsh, and K. Widener, 1998: An unattended cloud-profiling radar for use in climate research. *Bull. Amer. Meteor. Soc.,* **79,** 443–455.

Morrison, H., G. de Boer, G. Feingold, J. Harrington, M. D. Shupe, and K. Sulia, 2012: Resilience of persistent Arctic mixed-phase clouds. *Nat. Geosci.,* **5,** 11–17.

Neff, W. D., D. Helmig, A. Grachev, and D. Davis, 2008: A study of boundary layer behavior associated with high NO concentrations at the South Pole using a minisodar, tethered balloon, and sonic anemometer. *Atmos. Environ.,* **42,** 2762–2779.

Nicholls, R. J., and A. Cazenave, 2010: Sea-level rise and its impact on coastal zones. *Science,* **328,** 1517–1520.

O'Connor, E. J., R. J. Hogan, and A. J. Illingworth, 2005: Retrieving stratocumulus drizzle parameters using Doppler radar and lidar. *J. Appl. Meteor.,* **44,** 14–27.

Pinto, J. O., 1998: Autumnal mixed-phase cloudy boundary layers in the Arctic. *J. Atmos. Sci.,* **55,** 2016–2038.

Putnins, P., 1970: The climate of Greenland. *World Survey of Climatology,* Vol. 14, E. Landsberg, Ed., Elsevier, 3–128.

Rathke, C., J. Fischer, S. Neshyba, and M. D. Shupe, 2002: Improving IR cloud phase determination with 20 microns spectral observations. *Geophys. Res. Lett.,* **29,** 1209, doi:10.1029/2001GL014594.

Ridley, J. K., P. Huybrechts, J. M. Gregory, and J. A. Lowe, 2005: Elimination of the Greenland Ice Sheet in a high CO_2 climate. *J. Climate,* **18,** 3409–3427.

Rignot, E., and P. Kanagaratnam, 2006: Changes in the velocity structure of the Greenland Ice Sheet. *Science,* **311,** 986–990.

Rose, T., S. Crewell, U. Löhnert, and C. Simmer, 2005: A network suitable microwave radiometer for operational monitoring of the cloudy atmosphere. *Atmos. Res.,* **75,** 183–200.

Sassen, K., 1974: Depolarization of laser light backscattered by artificial ice clouds. *J. Appl. Meteor.,* **13,** 923–933.

——, and B. S. Cho, 1992: Subvisual-thin cirrus lidar dataset for satellite verification and climatological research. *J. Appl. Meteor.,* **31,** 1275–1285.

Schuenemann, K. C., J. J. Cassano, and J. Finnis, 2009: Synoptic forcing of precipitation over Greenland: Climatology for 1961–99. *J. Hydrometeor.,* **10,** 60–78.

Scorer, R. S., 1988: Sunny Greenland. *Quart. J. Roy. Meteor. Soc.,* **114,** 3–29.

Sedlar, J., M. D. Shupe, and M. Tjernström, 2012: On the relationship between thermodynamic structure and cloud top, and its climate significance in the Arctic. *J. Climate,* **25,** 2374–2393.

Sheppard, B. E., and P. I. Joe, 2008: Performance of the Precipitation Occurrence Sensor System as a precipitation gauge. *J. Atmos. Oceanic Technol.,* **25,** 196–212.

Shupe, M. D., 2007: A ground-based multisensor cloud phase classifier. *Geophys. Res. Lett.,* **34,** L22809, doi:10.1029/2007GL031008.

——, T. Uttal, and S. Y. Matrosov, 2005: Arctic cloud microphysics retrievals from surface-based remote sensors at SHEBA. *J. Appl. Meteor.,* **44,** 1544–1562.

——, S. Y. Matrosov, and T. Uttal, 2006: Arctic mixed-phase cloud properties derived from surface-based sensors at SHEBA. *J. Atmos. Sci.,* **63,** 697–711.

——, P. Kollias, M. Poellot, and E. Eloranta, 2008: On deriving vertical air motions from cloud radar Doppler spectra. *J. Atmos. Oceanic Technol.,* **25,** 547–557.

——, V. P. Walden, E. Eloranta, T. Uttal, J. R. Campbell, S. M. Starkweather, and M. Shiobara, 2011: Clouds at Arctic atmospheric observatories, Part I. Occurrence and macrophysical properties. *J. Appl. Meteor. Climatol.,* **50,** 626–644.

Solomon, A., M. D. Shupe, P. O. G. Persson, and H. Morrison, 2011: Moisture and dynamical interactions maintaining Arctic decoupled mixed-phase stratocumulus in the presence of a humidity inversion. *Atmos. Chem. Phys.,* **11,** 10 127–10 148.

Stamnes, K., R. G. Ellingson, J. A. Curry, J. E. Walsh, and B. D. Zak, 1999: Review of science issues, deployment strategy, and status for the ARM North Slope of Alaska–Adjacent Arctic Ocean climate research site. *J. Climate,* **12,** 46–63.

Starkweather, S. M., 2004: Characteristics of cloud cover and its radiative impacts over the high elevations of the Greenland Ice Sheet. Ph.D. dissertation, University of Colorado, 202 pp.

Steffen, K., and J. Box, 2001: Surface climatology of the Greenland Ice Sheet: Greenland Climate Network 1995–1999. *J. Geophys. Res.,* **106** (D24), 33 931–33 964.

Stroeve, J., M. M. Holland, W. Meier, T. Scambos, and M. Serreze, 2007: Arctic sea ice decline: Faster than forecast. *Geophys. Res. Lett.,* **34,** L09501, doi:10.1029/2007GL029703.

Tedesco, M., 2006: Greenland Ice Sheet snowmelt from spaceborne microwave brightness temperatures. *Eos, Trans. Amer. Geophys. Union,* **88,** 238, doi:10.1029/2007EO220003.

Tjernström, M., and Coauthors, 2012: Meteorological conditions in the central Arctic summer during the Arctic Summer Cloud Ocean Study (ASCOS). *Atmos. Chem. Phys.,* **12,** 6863–6889, doi:10.5194/acp-12-6863-2012.

Turner, D. D., 2005: Arctic mixed-phase cloud properties from AERI lidar observations: Algorithm and results from SHEBA. *J. Appl. Meteor.,* **44,** 427–444.

——, 2007: Improved ground-based liquid water path retrievals using a combined infrared and microwave approach. *J. Geophys. Res.,* **112,** D15204, doi:10.1029/2007JD008530.

——, and E. W. Eloranta, 2008: Validating mixed-phase cloud optical depth retrieved from infrared observations with high spectral resolution lidar. *IEEE Geosci. Remote Sens. Lett.,* **5,** 285–288, doi:10.1109/LGRS.2008.915940.

——, W. F. Feltz, and R. A. Ferrare, 2000: Continuous water vapor profiles from operational ground-based active and passive remote sensors. *Bull. Amer. Meteor. Soc.,* **81,** 1301–1317.

——, S. A. Ackerman, B. A. Baum, H. E. Revercomb, and P. Yang, 2003: Cloud phase determination using ground-based AERI observations at SHEBA. *J. Appl. Meteor.,* **42,** 701–715.

——, S. A. Clough, J. C. Liljegren, E. E. Clothiaux, K. Cady-Pereira, and K. L. Gaustad, 2007a: Retrieving liquid water path and precipitable water vapor from Atmospheric Radiation Measurement (ARM) microwave radiometers. *IEEE Trans. Geosci. Remote Sens.,* **45,** 3680–3690.

——, and Coauthors, 2007b: Thin liquid water clouds: Their importance and our challenge. *Bull. Amer. Meteor. Soc.,* **88,** 177–190.

Uttal, T., and Coauthors, 2002: Surface Heat Budget of the Arctic Ocean. *Bull. Amer. Meteor. Soc.,* **83,** 255–276.

Vaughan, M. A., and Coauthors, 2009: Fully automated detection of cloud and aerosol layers in the CALIPSO lidar measurements. *J. Atmos. Oceanic Technol.,* **26,** 2034–2050.

Wang, X., and J. R. Key, 2005: Arctic surface, cloud, and radiation properties based on the AVHRR Polar Pathfinder dataset. Part I: Spatial and temporal characteristics. *J. Climate,* **18,** 2558–2574.

Zhang, X., A. Sorteberg, J. Zhang, R. Gerdes, and J. Comiso, 2008: Recent radical shifts of atmospheric circulations and rapid changes in Arctic climate system. *Geophys. Res. Lett.,* **35,** L22701, doi:10.1029/2008GL035607.